CDF/ANAL/ELECTROWEAK/CDFR/9328

An Improved Measurement of the W Boson Mass with CDF in Run II : First Plots of the Data

Dan Beecher, Ilija Bizjak, Mark Lancaster, Sarah Malik, Emily Nurse, Tom Riddick, Dave Waters

University College London

Chris Hays, Peter Renton, Oliver Stelzer-Chilton

University of Oxford

Bo Jayatilaka, Ashutosh Kotwal, Ravi Shekar, Yu Zeng

Duke University

Larry Nodulman

Argonne National Laboratory

Abstract

Based on the experience with the first CDF Run II W mass and width measurements, two approaches to the simulation of the weak boson production, decay and detector effects are being used for the improved measurement of the W mass in approximately 2.4 fb^{-1} of CDF Run II $p\bar{p}$ data. We present a set of fits to the invariant mass distributions of J/Ψ and $\Upsilon(1S)$ events and Z and W boson kinematical distributions, which show that the description by the two simulations is still satisfactory even with ten times more data.

Contents

1 Introduction

The current measurement follows a very successful pair of measurements of the W mass [1] (200 pb^{-1}) and width [2] (350 pb^{-1}) on the CDF Run II data. Both measurements are the single most precise measurements of its quantity to date, and have developed and used for the measurement two independent fast simulations and parameterizations of weak boson production, decay and detector response. The two simulations, applied to the measurement of the W mass, can now be used to cross-check each other's results and thus allow for a critical assessment of different simulation methods of relevant processes involved in the W mass measurement.

Both simulations have been developed and tuned on significantly smaller data-samples than we have at hand today, raising the question whether the solutions that worked then can successfully simulate the much larger data sample with more than three times the statistical resolution of the previous samples.

The larger data samples also span a longer data-taking period, which introduces possible time-dependent effects (ageing and mis-alignment of the detector) and includes a larger variety of changes applied to the detector over time. Last but not least, the Tevatron has gradually increased the luminosity of $p\bar{p}$ collisions (See Fig. 1 for instant luminosity distribution comparison), which affects the shapes and quantities of underlying events, multiple interactions and backgrounds, and require the introduction of new solutions to successfully trigger on most interesting data.

The following note explains the changes and improvements to the alignment of the data and the event simulation, applied since the completion of the previous two measurements. By comparing the outcome of the two simulations to the data distributions we conclude that the two simulations are on the right track to achieve the goal W mass measurement accuracy of 25 MeV/c^2.

1.1 Datasets

The data used in the following analysis span CDF data periods $0-13$ (0d to 0i, including part of 0j), the data taken between 04 Feb 02 and 4 Aug 07. The integrated luminosity of the data, excluding events that have been flagged as bad, is 2.4 fb^{-1} and 2.3 fb^{-1}, for high momentum electron and muon candidates respectively. The data includes the samples used in the aforementioned published measurements.

Additional datasets of cosmic, minbias, zerobias, Υ and J/ψ events were used for the same data-taking period.

2 Event Selection

The event selection follows closely the selection described in [1]. A short summary of the event selection criteria is given in Tables 1 and 2.

The lepton candidates in Z decays have an additional upper bound on p_T of $p_T <$ 65 GeV/c to make it consistent with the lepton candidates from W bosons.

all leptons	$\|z_0\| < 60$ cm $30 < p_T < 65$ GeV/c 4 axial + 4 stereo SL (at least 5 hits each) All COT layers
Muons	$\|d_0\| < 0.1$ cm $\chi^2 < 3$ $E_{EM} < 2$ GeV $E_{HAD} < 6$ GeV dx(cmu,cmp,cmx) $< (3, 5, 6)$ cm
Electrons	$p_T^{(\text{track})} < 18$ GeV/c $E/pc < 2$ $\|\text{CES}\, x\| < 18$ cm $12 < \|\text{CES}\, z\| < 230$ cm $E_{HAD}/E_{EM} < 0.1$ $L_{shr} < 0.3$ $\|\Delta z\| < 5$ cm Fiducial, exclude tower 9

Table 1: Lepton selection requirements.

The tracking isolation requirement has been removed from the Z-vetoing criteria, since it was biasing against events with higher number of COT hits.

3 Data alignment

To improve tracking resolution, the COT alignment was performed using cosmic ray data from the entire data period (see Section 1.1). Requiring exactly two reconstructed tracks on opposite sides of the COT representing a single cosmic ray muon, the two tracks are fitted to a single helical track and the residuals are calculated for each cell. Each cell position is then aligned by a shift along the global azimuth and a tilt around its center to minimize the residuals.

Tracks are also corrected based on the difference of the means of the E/pc distributions for electrons and positrons in the $W \to e\nu$ data. The curvature correction is derived in powers of $\cot\theta$ and harmonics of $\sin\phi$:

$$\delta c = a_0 + a_1 \cot\theta + a_2 \cot^2\theta + b_1 \sin(\phi + \phi_{01}) + b_2 \sin(3\phi + \phi_{02}) \quad . \tag{1}$$

The obtained parameters are summarized in Table 3.

Z candidates	$66 < m_Z < 116$ GeV/c^2
	$\lvert\Delta T_0\rvert < 4$
	$p_T^Z < 30$ GeV/c
	Standard cosmic veto (muons only)
W candidates	$60 < m_T < 100$ GeV/c^2
	$30 < \not\!\!E_T < 55$ GeV
	$p_T^\ell < 55$ GeV/c
	$U < 15$ GeV/c
	Standard cosmic veto (muons only)

Table 2: Event selection requirements.

	$\times 10^{-5}\text{cm}^{-1}$	
a_0	1.3 ± 0.2	
a_1	9.0 ± 0.4	
a_2	5.8 ± 0.4	
b_1	29 ± 1	
b_2	6 ± 1	runs before 212133
b_2	4 ± 3	runs after 212133

ϕ_{01}	α	
ϕ_{02}	β_1	runs before 212133
ϕ_{02}	β_2	runs after 212133

Table 3: The track curvature corrections based on the difference of the means of the E/pc distributions for electrons and positrons in $W \to e\nu$ data.

4 Simulation

We use two independent simulation frameworks, `Simulation-I` and `Simulation-II` , described in detail in Refs. [1] and [2], respectively. A short summary of the two simulations follows, describing the improvements and the work done since the previous measurements.

4.1 Event generation

`Simulation-I` uses `RESBOS` [3] coupled with `WGRAD` [4] to generate the 2-body weak boson decay and up to one photon. The weak boson p_T is modelled by `RESBOS`, which describes the NLO initial state QCD effects (finite boson p_T and leptonic angular distribution), while the final-state QED photon contribution is sampled using distributions obtained with `WGRAD`.

`Simulation-II` uses `Horace-3.1` generator [5] for the simulation of the electro-weak corrections to the production and the decay of the electro-weak bosons. The generator implements the exact $\mathcal{O}(\alpha)$ calculation matched with the leading-Sudakov-logarithm QED parton shower simulation of additional photons. The boson p_T due to initial state QCD effects is added by boosting the boson-decay products based on a distribution calculated with `RESBOS`, using the BLNY parameterization [6] of the non-perturbative effects at low p_T.

Both simulations are able to use different Parton Distribution Functions (PDF) to study the PDF dependence of the result. The default in use is `CTEQ6M` [7].

4.2 Detector simulation

Both simulations have to resort to a parameterized model of the detector to allow generation of the number of events needed for a successful measurement of the W mass.

4.2.1 Beam pipe and Silicon detector

The ionization losses of muons and electrons and bremsstrahlung losses of electrons are modelled using a mapping of the material up to the COT. The effects of multiple and Compton scatterings are also taken into account.

New to `Simulation-II` since the published analysis is the simulation of the energy loss of photons due to the Compton scattering in the silicon detector and the implementation of the Migdal suppression of bremsstrahlung for low E_γ/E_e.

The amount of material used in the simulation of energy loss in transition through the detector is tuned in the fit to the high E/pc tail of $W \to e\nu$ events, by scaling the radiation length X_0 by a material scale S^{mat}.

4.2.2 COT and Momentum measurement

`Simulation-I` implements a hit-level description (hit resolution and (in-)efficiency) of the tracking in the COT, and also simulates the helical track fit. A super-layer-dependent COT hit resolution was introduced to accommodate for a gradual worsening of the hit

resolution with the higher occupancy in the innermost super-layers. The hit resolutions are obtained on $\Upsilon(1S) \to \mu^+\mu^-$ data and are summarized in Table 4.

	SL1	SL2	SL3	SL4	SL5	SL6	SL7	SL8
COT hit resolution (μm)	181	158	163	148	150	144	144	142

Table 4: COT hit resolution for each super-layer.

The beam spot size σ_b acts as an effective "hit" resolution of the additional point on the track when beam-constraining the track fit. Since the low-momentum tracks from $\Upsilon(1S)$ decays are affected by multiple scattering in the silicon, the beam spot size is measured separately in the $Z \to \mu^+\mu^-$ decays to be $\sigma_b = (43 \pm 3)$ μm.

`Simulation-II` describes momentum measurement starting on the track level (no hit simulation) by sampling the momentum resolution based on the full CDF detector simulation (CDFSim), where an additional smearing parameter, $S^{\rm res}$, is tuned in fits to the Z invariant mass distribution of $Z \to \mu^+\mu^-$ events. For electrons it also simulates the effect on the momentum measurement due to the bremsstrahlung radiation in the first half of the COT (in radial direction). The description of the z_0 distribution of the tracks in `Simulation-II` has been improved by including the information of the beam parameter changes for 115 different data run ranges.

Both simulations use the absolute momentum scale from fits to the invariant mass distributions of $\Upsilon(1S) \to \mu^+\mu^-$, $J/\psi \to \mu^+\mu^-$ and $Z \to \mu^+\mu^-$ events (see Sec. 5).

4.2.3 Calorimeter simulation

The muon ionization losses deposited in the calorimeter are described based on measurements in data with single cosmic track events.

Both simulations remove from further analysis (recoil) the energy measurement in a region of 7 towers for electrons and 3 towers for muons around the lepton tower. The energy deposition of the additional underlying activity in those towers is measured in $W \to \ell\nu$ events away from the charged lepton tower and are: subtracted in the simulation as a function of $u_{||}$, $u_\perp$ and track η for `Simulation-I`, or added back to the data as a function of the instant luminosity $\mathcal{L}$, $u_{||}$ and tower η for `Simulation-II`.

The energy deposition of electrons and photons in the Electro-Magnetic (EM) calorimeter (with the losses in the coil and TOF) and the leakage of energy into the Hadronic calorimeter are modelled using `GEANT` simulation of the CDF detector. `Simulation-II` uses a tower-dependent (η) parameterization of the energy leakage.

Both simulations takes into account the non-linear calorimeter response (dependence of the response on the deposited energy) and scale the energy measurements by an absolute energy scale. The amount of non-linearity and the absolute energy scale are tuned in the fits to the E/pc distributions of electrons in $W \to e\nu$ events.

The calorimeter resolution is modelled by smearing the simulated energies with a

normal distribution with standard deviation σ_E

$$\sigma_E^2 = \left(13.5\%/\sqrt{E_T}\right)^2 + \kappa^2 \quad . \tag{2}$$

`Simulation-I` additionally smears the energies of secondary particles (photons and conversion electrons) by $\kappa_2 = 8.3 \pm 2\%$. κ_2 is measured in a fit to the $Z \to e^+e^-$ invariant mass distribution for events with high E/pc ($E/p > 1.06$). This significantly improves the agreement of the values of primary κ (Eq. 2) obtained from E/pc and $Z \to e^+e^-$ invariant mass fits.

4.2.4 Recoil

The energy depositions in the calorimeter that are not associated with the primary charged lepton(s) are referred to as the recoil. They are caused by particles from initial state QCD radiation, the hadronization of the $p\bar{p}$ remnants not partaking in the boson creation, multiple collisions from the same bunch crossing and conversions from photons interacting with the detector material.

Both simulations study the recoil by observing the spatial components in the boson direction ($U_{||}$) and in the direction perpendicular to the boson ($U_\perp$) (`Simulation-I` uses coordinates relative to the bisector of the angle between the two prompt leptons). The *recoil response* is then the strongly p_T-dependent recoil component balancing the boson p_T, while the component perpendicular to the boson direction has zero mean response since the underlying event should be decoupled from boson direction. Recoil response is in both simulations parametrized as a function of the boson p_T. The *recoil resolution*, the spread of measured recoil energies, is simulated as follows.

`Simulation-I` separates the recoil into three components: radiation coming from the boson production, radiation from spectator partons and energy from additional collisions in a given bunch crossing. The boson production contribution has a boson p_T dependence and is tuned to the Z data, minbias data is used for spectator-parton contribution, while the recoil component from multiple interactions is based on the zerobias sample. The resolution is modelled as a function of the $\sum E_T$ distribution. Single-collision $\sum E_T$ is obtained by deconvoluting the distribution of the number of collisions from the total $\sum E_T$ in zerobias data. A $\sum E_T$ scale N_Z [1] takes into account the difference between the $\sum E_T$ in zerobias data and $W(Z)$ data, and was obtained to be $N_Z = 1.278$. The stochastic term in the p_T dependent resolution has also been re-tuned and is consistent to the published value [1].

`Simulation-II` takes a different approach by parameterizing the mean and the spread of the $\sum E_T$ in Z events as a function of the instant luminosity $\mathcal{L}$ and the p_T of the boson. The $\sum E_T$ is generated according to the *gamma distribution* with its mean and the standard deviation parameterized as:

$$\langle \Sigma E_T \rangle = a_0 + a_1 \times p_T + a_2 \times \mathcal{L} \tag{3}$$

$$\sigma(\Sigma E_T) = b_0 + b_1 \times p_T + b_2 \times \mathcal{L}^{\,0.48} \tag{4}$$

The parameters $a_{1,2,3}$ and $b_{1,2,3}$ are obtained by minimizing the sum of the χ^2 values for $\langle \Sigma E_T \rangle$ vs. p_T, $\langle \Sigma E_T \rangle$ vs. $\mathcal{L}$, $\sigma(\Sigma E_T)$ vs. p_T, $\sigma(\Sigma E_T)$ vs. $\mathcal{L}$ and the ΣE_T distribution on $Z \to \ell^+\ell^-$ events (the parameters are obtained separately for $Z \to \mu^+\mu^-$ and $Z \to e^+e^-$ events). The comparison of the data ΣE_T distributions with the prediction using `Simulation-II` for events with instant luminosity higher and lower than 70×10^{30} s^{-1} cm^{-2} (chosen to correspond to the mean instant luminosity (69.4×10^{30} s^{-1} cm^{-2})), shows a good agreement in both ranges (See Fig. 1(b) for the example of $Z \to e^+e^-$ events).

The resolution of the recoil is then parameterized as a function of $\sum E_T$, where the luminosity dependence of the recoil is captured in the parameterization of ΣE_T (Eqs. 3 and 4).

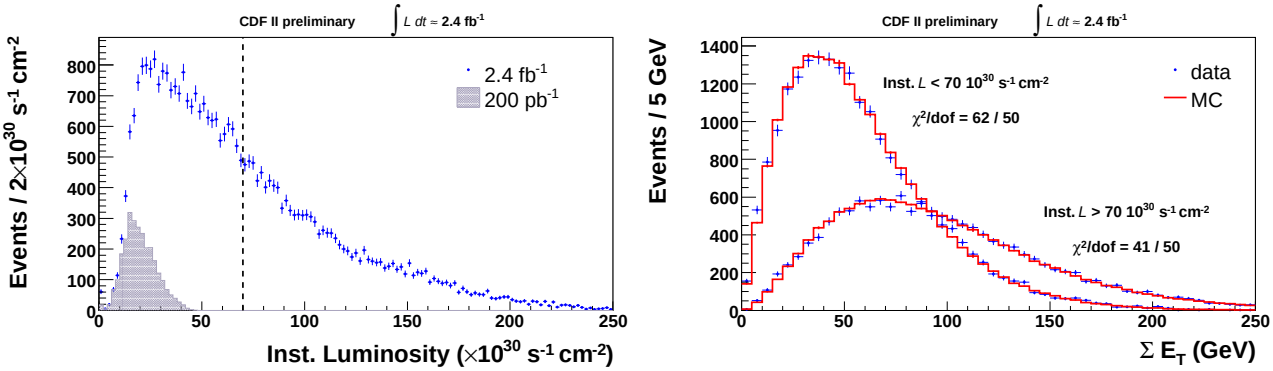

(a) (b)

Figure 1: (a) Instant luminosity $\mathcal{L}$ comparison for the 200 pb^{-1} and 2.4 fb^{-1} samples of $Z \to e^+e^-$ candidate events. The vertical line represents 70×10^{30} s^{-1} cm^{-2}, the value corresponding to the average instantaneous luminosity. (b) The comparison of the data ΣE_T distributions for $Z \to e^+e^-$ candidates with the prediction using `Simulation-II` for high ($\mathcal{L} > 70 \times 10^{30}$ s^{-1} cm^{-2}) and low ($\mathcal{L} < 70 \times 10^{30}$ s^{-1} cm^{-2}) luminosity events.

4.2.5 Backgrounds

Due to imperfect detector measurement and coverage, several background processes can mimic a $W \to \ell\nu$ decay, passing the W event selection. We have estimated the amounts and shapes of the dominant background contributions and add them to the simulation templates when performing kinematical fits.

The main backgrounds in the $W \to e\nu$ channel are $Z \to e^+e^-$ and $W \to \tau\nu$ events, and events where a hadronic jet was reconstructed as the lepton (multi-jet background). We model $Z \to e^+e^-$ and $W \to \tau\nu$ events using `Pythia` and the detector using CDFSim. We model the multi-jet background in a sample where the $\not\!\!E_T$ requirement is removed (see Table 2), by fitting the fraction of the parameterized multi-jet events together with

the expected $W \to e\nu$ channel are $Z \to e^+e^-$ and $W \to \tau\nu$ contributions to the observed distribution.

The main backgrounds in the $W \to \mu\nu$ channel are $Z \to \mu^+\mu^-$ and $W \to \tau\nu$ events, cosmic rays, decays of low momentum pions or kaons into muons in the COT, and hadronic jets, penetrating into the muon chambers. The $Z \to \mu^+\mu^-$ and $W \to \tau\nu$ events are modelled using `Pythia`and the detector response using CDFSim. The contribution of low momentum meson decays is estimated in the sample of muon candidates having either a large track χ^2 or a large d_0, and then extrapolated into the signal region. The amount of hadronic background is estimated in the distributions of track and calorimeter isolation variables, by observing the exceess after taking into account the expected $W \to e\nu$, $Z \to e^+e^-$ and $W \to \tau\nu$ contributions to the observed distributions.

5 Momentum scale fits

The determination of the absolute momentum scale is one of the most important aspects of the W mass measurement, since scaling the measured momenta directly shifts the fitted kinematical distributions, biasing the measured mass of the W boson.

The effect of the momentum scale on the measured mass can be used to set the absolute momentum scale in the measurement of precisely known masses of the Z boson ($m_Z = 91187.6 \pm 2.1$ MeV/c^2 [8]) and resonances J/ψ ($m_{J/\psi} = 3096.916 \pm 0.011$ MeV/c^2 [8]) and $\Upsilon(1S)$ ($m_{\Upsilon(1S)} = 9460.30 \pm 0.26$ MeV/c^2 [8]).

Since the momentum scale can be measured more accurately than the absolute energy scale (assuming that the momentum scale of the COT measurement is the same for electrons and muons), the electron E/pc distribution can be used to calibrate the energy scale using the momentum scale.

The fits to the invariant mass distributions of resonances J/ψ and $\Upsilon(1S)$ are presented in this section, while the Z mass fits are shown in Section 6.

5.1 $J/\psi \to \mu^+\mu^-$ and $\Upsilon(1S) \to \mu^+\mu^-$ event simulation

We use `Pythia` [9] event generator to generate the $J/\psi \to \mu^+\mu^-$ and $\Upsilon(1S) \to \mu^+\mu^-$ decays. The QED radiation of the muons in the quarkonia decays, not simulated in `Pythia`, is added in the leading-Sudakov-logarithm approximation. The `Pythia` output is tuned by adjusting the boost of the decay products in the $p_T^{\mu^+\mu^-}$ direction and the θ^* angle of the muons in the rest-frame of the decaying quarkonium.

The detector simulation includes the propagation through detector material and COT hit reconstruction using SL-dependent hit resolutions and hit efficiencies (efficiencies are separately measured for $J/\psi \to \mu^+\mu^-$ and $\Upsilon(1S) \to \mu^+\mu^-$ decays).

A set of curvature corrections is calculated for quarkonia on the sample of $J/\psi \to \mu^+\mu^-$ decays, and then applied to the $\Upsilon(1S) \to \mu^+\mu^-$ data. The observed quadratic dependence of the momentum scale as a function of $\Delta \cot\theta$, the angle between the two muons in the decay, is removed by introducing the following corrections:

$$\delta c = (1.9 \times 10^{-7}\mathrm{cm}^{-1}) \times \cot\theta \quad (5)$$

$$\delta \cot\theta = (1.76 \times 10^{-3}) \times \cot\theta \quad (6)$$

$$(7)$$

These corrections are only applied to the $J/\psi \to \mu^+\mu^-$ and $\Upsilon(1S) \to \mu^+\mu^-$ data, while the curvature corrections derived from $W \to e\nu$ $\langle E/pc \rangle$ difference for electrons and positrons (Eq. 1) are not applied here.

5.2 $J/\psi \to \mu^+\mu^-$ fits

The momenta of the muons in the $J/\psi \to \mu^+\mu^-$ decays are on average much lower than those in Z and W decays. To extrapolate the momentum scale measurement to

large momenta (low curvature), we fit the invariant mass in bins of mean curvature ($0.1 < \langle 1/p_T^{\mu} \rangle < 0.5$ GeV/c^{-1} in steps of 0.05 GeV/c^{-1}).

Since the energy losses affect the momentum scale differently for different average muon momenta, the amount of the ionizing material in the simulation is scaled by E_I to flatten out any dependence of the obtained momentum scales on the track curvatures. The ionization scale E_I is consistent to the one obtained on 200 pb^{-1} ($E_I = 0.94$).

The momentum scale in the $J/\psi \to \mu^+\mu^-$ events is fitted in three steps for each curvature bin: first we double the fit range ($2.82 - 3.34$ GeV/c^2) and fit for the background contribution, which is simulated as a linear slope; in this fit the momentum resolution and scale are left floating (the dependence of the background on the two is small). Next we fix the background shape and fit for the momentum resolution, while the momentum scale is floating. Last, we fit for the momentum scale in the mass range of $2.95 - 3.21$ GeV/c^2, where the background component and the momentum resolution are fixed to the previously obtained values, and the total number of events is fixed to the number of events in data.

The curvature measurement has been corrected on data using equations 5,6 and the simulation uses SL-dependent hit resolution (see Table 4).

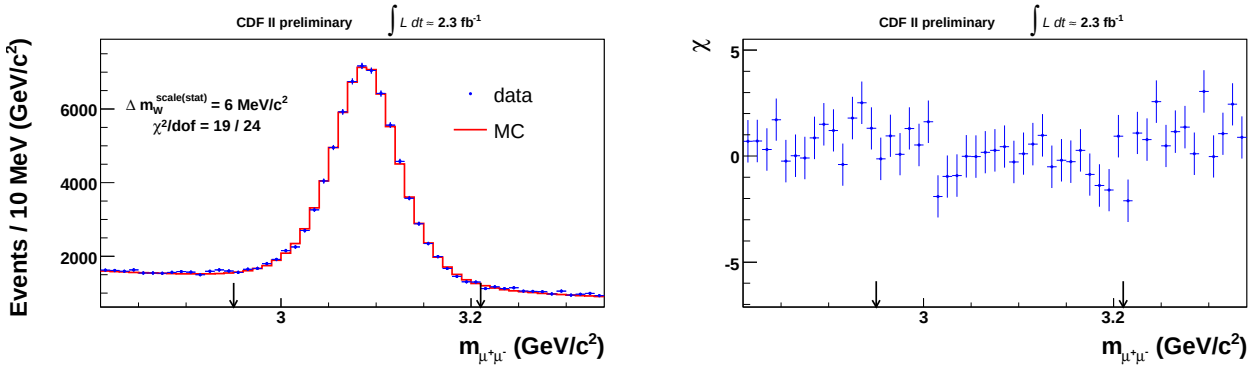

(a) (b)

Figure 2: (a) The $J/\psi \to \mu^+\mu^-$ mass ($m_{\mu^+\mu^-}$) plot for the highest momentum bin ($6.7 < \langle p_T \rangle < 10$ GeV/c). The plot window corresponds to the fit window used for background estimation, and the arrows indicate the fit window for the momentum scale fit. (b) The difference between the data and simulation (χ) in each bin.

5.3 $\Upsilon(1S) \to \mu^+\mu^-$ fits

The higher average muon momenta in $\Upsilon(1S) \to \mu^+\mu^-$ decays make the $\Upsilon(1S)$ momentum scale measurement less sensitive to the details of the the QED simulation and ionizing material than the measurement in $J/\psi \to \mu^+\mu^-$, which causes the precision on the momentum scale determined in $\Upsilon(1S) \to \mu^+\mu^-$ decays to be comparable to that obtained on

	χ^2	p.val.	$\Delta m_W^{\text{scale(stat.)}}$
200 pb^{-1}	49/24	0.2%	20 MeV/c^2
2300 pb^{-1}	19/24	75 %	6 MeV/c^2

Table 5: The $J/\psi \to \mu^+\mu^-$ mass ($m_{\mu^+\mu^-}$) fit for the highest momentum bin ($6.7 < \langle p_T \rangle < 10$ GeV/c): the fit quality and the uncertainty on the M_W due to the statistical uncertainty of the fit on the momentum scale.

the much larger $J/\psi \to \mu^+\mu^-$ sample. Since $\Upsilon(1S)$ is produced in the proton collisions (approximately 20% of J/ψ candidates are produced in the B meson decays), the momentum scale can be determined using beam-constrained (BC) track fits. The comparison of the obtained momentum scales for the case of BC and non-BC fits is used to estimate the possible BC bias on the momentum scale measurement.

The fits of the invariant mass follow the method described for the J/ψ fits: the background is simulated as a linear slope and is determined in the fit range of $9.13 - 9.73$ GeV/c^2; in this fit the momentum resolution and scale are left floating (the dependence of the background on the two is small). Next we fix the background shape and fit for the momentum resolution, while the momentum scale is floating. Last, we do a fit for the momentum scale in the mass range of $9.28 - 9.58$ GeV/c^2, where the background component and the momentum resolution are fixed to the previously obtained values, and the total number of events is fixed to the number of events in data.

The curvature measurement has been corrected on data using equations 5,6 and the simulation uses SL-dependent hit resolution (see Table 4).

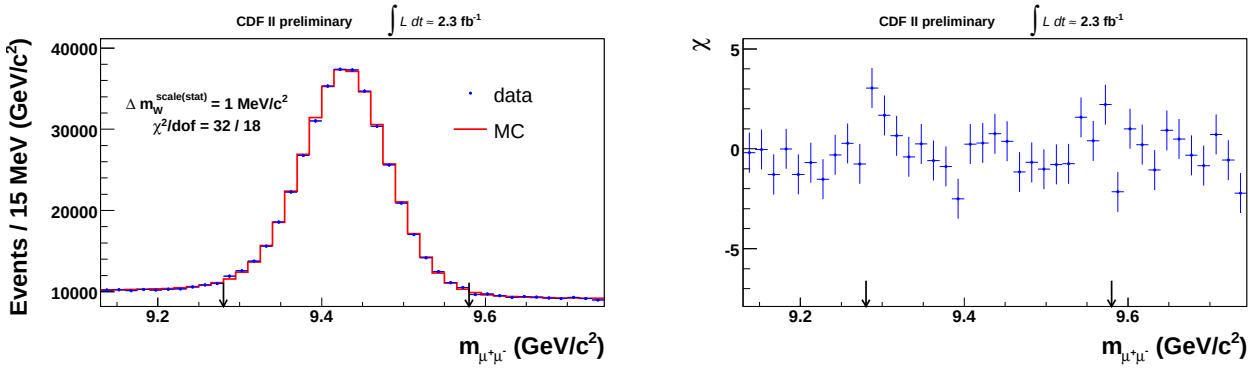

(a) (b)

Figure 3: (a) The $\Upsilon(1S) \to \mu^+\mu^-$ mass ($m_{e^+e^-}$) plot for the beam-constrained (BC) fit. The plot window corresponds to the fit window for background estimation, and the arrows indicate the fit window for the momentum scale fit. (b) The difference between the data and simulation (χ) in each bin.

	χ^2	p.val.	$\Delta m_W^{\text{scale(stat.)}}$
200 pb^{-1}	26/18	10%	4.8 MeV/c^2
2300 pb^{-1}	32/18	2%	1.5 MeV/c^2

Table 6: The $\Upsilon(1S) \to \mu^+\mu^-$ mass ($m_{\mu^+\mu^-}$) fit: the fit quality and the uncertainty on the M_W due to the statistical uncertainty of the fit on the momentum scale.

6 Z mass fits

6.1 $Z \to \mu^+\mu^-$ fits

For `Simulation-I`, a blind Z mass fit to the invariant mass of $Z \to \mu^+\mu^-$ candidates is performed (Figure 4(a,b)). The momentum resolution (σ_b, see Sec. 4.2) is obtained by a χ^2 fit to this plot. When the momentum scale is fixed from $J/\psi \to \mu^+\mu^-$ and $\Upsilon(1S) \to \mu^+\mu^-$ fits, the fit returns an absolute Z mass, otherwise it is effectively the fit for the absolute momentum scale.

For `Simulation-II`, a blind fit to the invariant mass of $Z \to \mu^+\mu^-$ is performed (Figure 4(c,d)), where the fitting parameters are the absolute momentum scale and the scaling factor S^{res} for the momentum smearing (Sec. 4.2). The fits to the two parameters are done iteratively for one parameter at the time, ending the iteration when the change in the two parameters falls below the statistical uncertainty. The uncertainty on the momentum scale is then converted to the uncertainty on the Z mass, assuming the relative uncertainty on the momentum scale is the relative uncertainty on the Z mass.

The fits give reasonable χ^2 probabilities (see Table 7). The uncertainty on m_Z, extrapolated by scaling the uncertainty at 200 pb^{-1}to the current integrated luminosity, is 13 MeV/c^2, compared to 12 MeV/c^2 obtained by the fit, from which we conclude that the error scales with statistics.

	`Simulation-I`			`Simulation-II`		
	χ^2	p.val.	$\Delta m_Z^{\text{stat.}}$(MeV/c^2)	χ^2	p.val.	$\Delta m_Z^{\text{stat.}}$(MeV/c^2)
200 pb^{-1}	33/30	32%	43			
2300 pb^{-1}	42/30	7%	12	28/30	57%	12

Table 7: $Z \to \mu^+\mu^-$ invariant mass fit: the comparison of the fit quality and the statistical uncertainty on the fitted parameter (m_Z) for the previous (200 pb^{-1}) and current iteration.

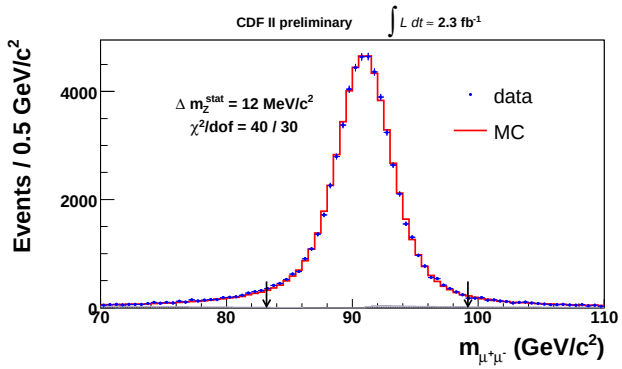

(a)

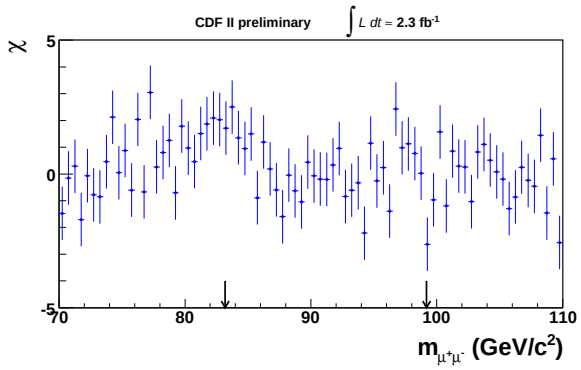

(b)

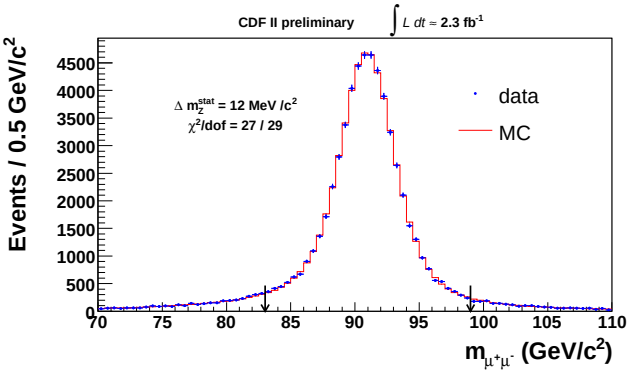

(c)

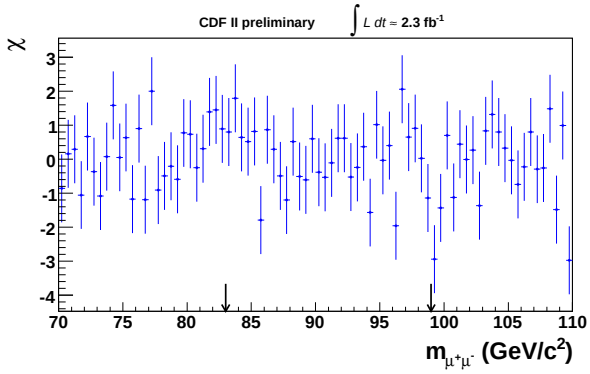

(d)

Figure 4: (a),(c) $Z \to \mu^+\mu^-$ invariant mass fit, and (b),(d) the difference between data and simulation (χ) in each bin, using `Simulation-I` and `Simulation-II`, respectively. The fit range is $83 < m_{\mu^+\mu^-} < 99\,\mathrm{GeV/c^2}$.

6.2 $Z \to e^+e^-$ fits

A blind Z mass fit is performed using `Simulation-I` to the reconstructed invariant mass of $Z \to e^+e^-$ candidates (Figure 5(a,b)). The absolute energy scale S_E and the primary energy resolution parameter $\kappa = (1.08 \pm 0.02_{(stat)})\%$ were determined by fitting the E/pc distribution, while the secondary parameter $\kappa_2 = (8.0 \pm 0.3)\%$ was obtained in the fit to the $Z \to e^+e^-$ invariant mass distribution for the sub-sample of events with $E/pc > 1.06$, assuming that the value of κ_2 does not depend strongly on the value of m_Z and letting its value float in the fit. The additional energy smearing parameter κ_2 is only applied to the secondary particles from radiation (photons and photon conversions in the material).

For `Simulation-II`, a blind fit to the invariant mass of $Z \to e^+e^-$ candidates is performed (Figure 5(c,d)), where the fitting parameters are the absolute energy scale and κ (no secondary κ is used). The fits to the two parameters are done iteratively for one parameter at the time, ending the iteration when the change in the two parameters falls below the statistical uncertainty. The uncertainty on the energy scale is then converted to the uncertainty on the Z mass.

The fits give reasonable χ^2 probabilities (see Table 8). The uncertainty on m_Z, extrapolated by scaling the uncertainty at 200 pb^{-1}to the current integrated luminosity, is 20 MeV/c^2 compared to 20 MeV/c^2 obtained by the fit, from which we conclude that the error scales with statistics.

	`Simulation-I`			`Simulation-II`		
	χ^2	p.val.	$\Delta m_Z^{\text{stat.}}$(MeV/c^2)	χ^2	p.val.	$\Delta m_Z^{\text{stat.}}$(MeV/c^2)
200 pb^{-1}	34/38	65%	67			
2400 pb^{-1}	51/38	8%	20	44/37	20%	20

Table 8: $Z \to e^+e^-$ invariant mass fit: the comparison of the fit quality and the statistical uncertainty on the fitted parameter (m_Z) for the previous (200 pb^{-1}) and current iteration.

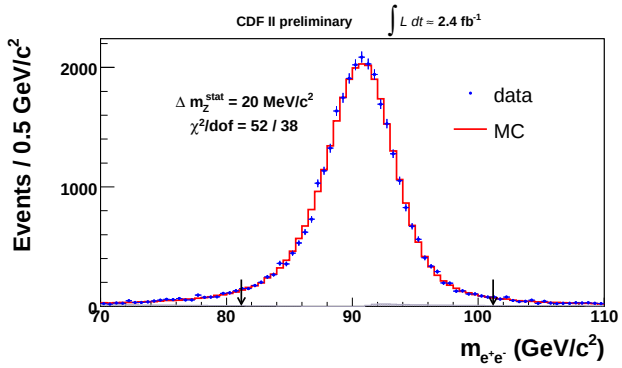

(a)

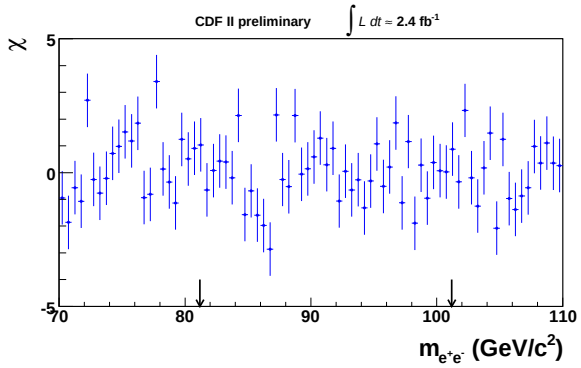

(b)

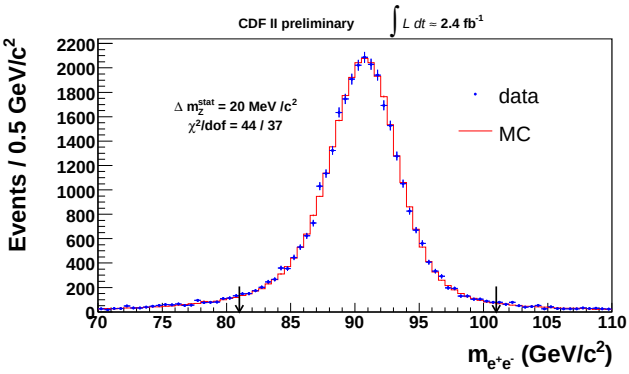

(c)

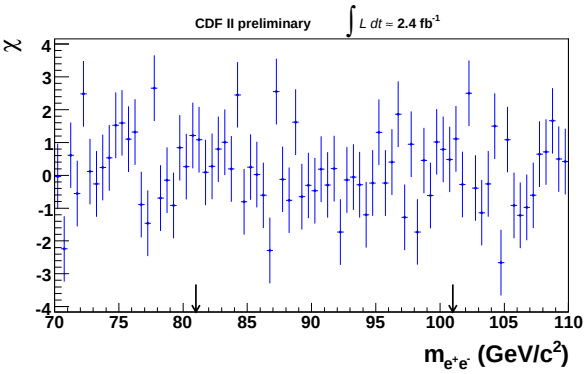

(d)

Figure 5: (a),(c) $Z \to e^+e^-$ invariant mass fit, and (b),(d) the difference between data and simulation (χ) in each bin, using `Simulation-I` and `Simulation-II`, respectively. The fit range is $81 < m_{e^+e^-} < 101\,\mathrm{GeV/c^2}$.

6.3 $Z \to e^+e^-$ fits using track information only

Electron momentum measurement is affected by the emission of photons due to bremsstrahlung. $Z \to e^+e^-$ track mass fit is therefore an important cross-check of the modelling of the energy losses in electrons.

The fits give reasonable χ^2 probabilities (see Table 9). The uncertainty on m_Z for the fit window of $60 < m_{e^+e^-} < 98\,\mathrm{GeV/c^2}$, extrapolated by scaling the uncertainty at 200 pb^{-1}to the current integrated luminosity, is 42 MeV/c^2, compared to 42 MeV/c^2 obtained from the fit, from which we conclude that the error scales with statistics.

	`Simulation-I`			`Simulation-II`		
	χ^2	p.val.	$\Delta m_Z^{\mathrm{stat.}}(\mathrm{MeV/c^2})$	χ^2	p.val.	$\Delta m_Z^{\mathrm{stat.}}(\mathrm{MeV/c^2})$
200 pb^{-1}	30/22	12%	143			
2400 pb^{-1}	27/22	21%	42	36/35	42%	39

Table 9: $Z \to e^+e^-$ invariant mass fit using track information only: the comparison of the fit quality and the statistical uncertainty on the fitted parameter (m_Z) for the previous (200 pb^{-1}) and current iteration. Note that `Simulation-II` fit has a different fit range.

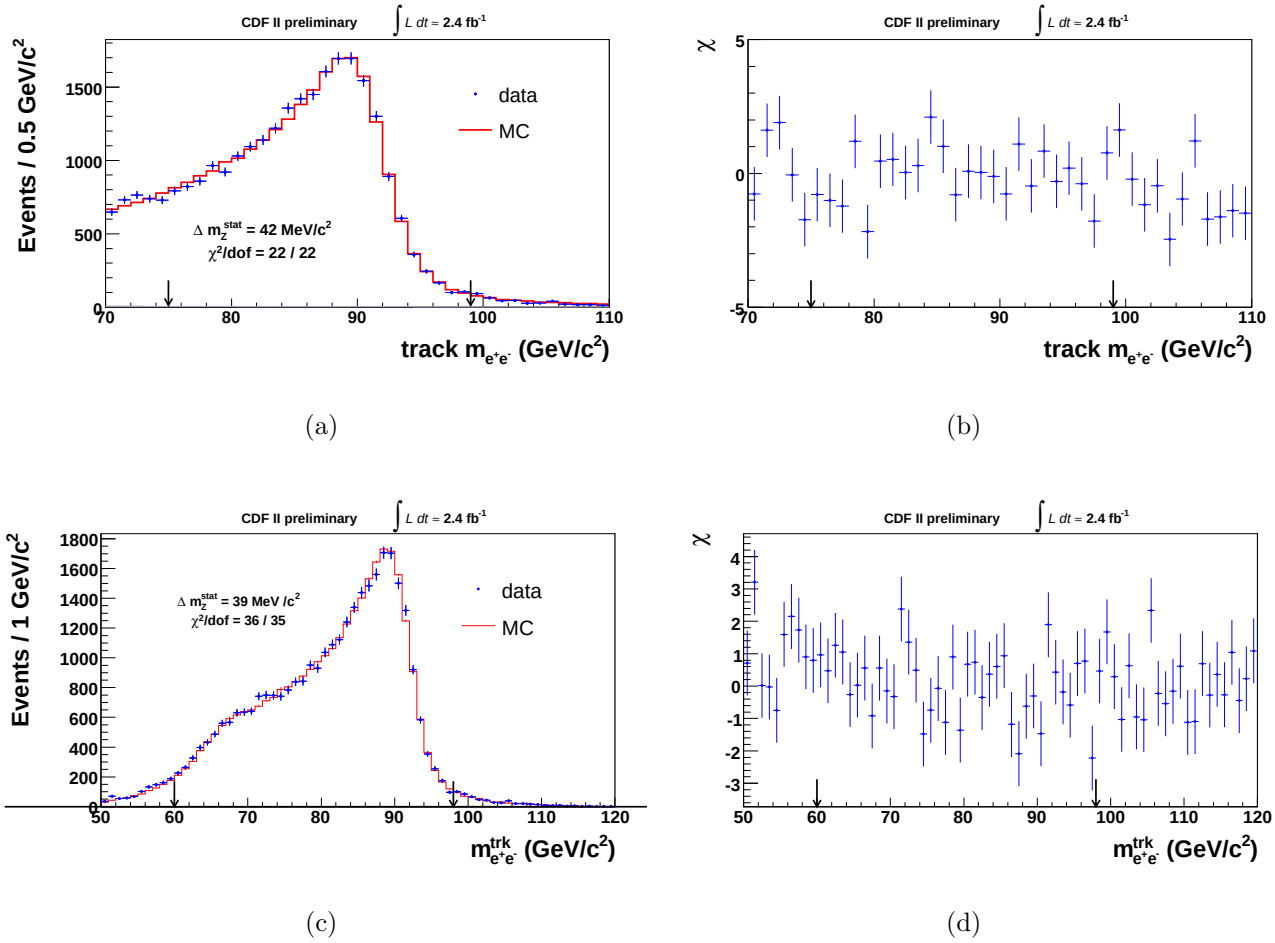

Figure 6: (a),(c) $Z \to e^+e^-$ invariant mass fit using track information only, and (b),(d) the difference between data and simulation (χ) in each bin, using `Simulation-I` and `Simulation-II`, respectively. The fit ranges are $75 < m_{e^+e^-} < 98\,\mathrm{GeV/c^2}$ for `Simulation-I` and $60 < m_{e^+e^-} < 98\,\mathrm{GeV/c^2}$ for `Simulation-II`.

7 Fits of kinematical distributions in $W \to \ell\nu$ events

The simulation of $W \to \ell\nu$ decays incorporates the measured momentum scales, tuned material scale $S^{\rm mat}$, and additionally for the electron channel the tune of energy measurement parameters: the non-linearity of response, the absolute scale and the energy smearing parameters κ and κ_2. The description of the unmeasured neutrino momentum, $\not\!\!E_T$, from the balance in the transverse plane is based on the recoil simulation (see Sec. 4.2.4), tuned on Z, minbias and zerobias data. The contribution from background processes (Sec. 4.2.5) that pass the W event-selection criteria (Sec. 2) is also estimated.

In this section we present the fits to the the E/pc and the *transverse mass* ($m_T = \sqrt{2p_T \cdot \not\!\!E_T \cdot [1 - \cos(\phi_\ell - \phi_\nu)]}$) distributions.

7.1 $W \to \mu\nu$ m_T fit

The transverse mass m_T distribution is fitted to a sum of background contribution and a set of templates with different input m_W. The templates are generated at a fixed m_W, and then re-weighted according to the relativistic Breit-Wigner distribution

$$\frac{d\sigma}{d\hat{s}} \propto \frac{1}{(\hat{s} - m_W^2)^2 + \hat{s}^2/m_W^2\Gamma_W^2} \quad . \tag{8}$$

The fit result is obtained by maximizing the likelihood for the bins of the m_T distribution, calculated with possion bin probabilities. The fitted value of m_W is blinded by an unknown shift, selected in the range of $\pm 75 \mathrm{MeV/c^2}$.

The background fractions and shapes are taken from Ref. [1].

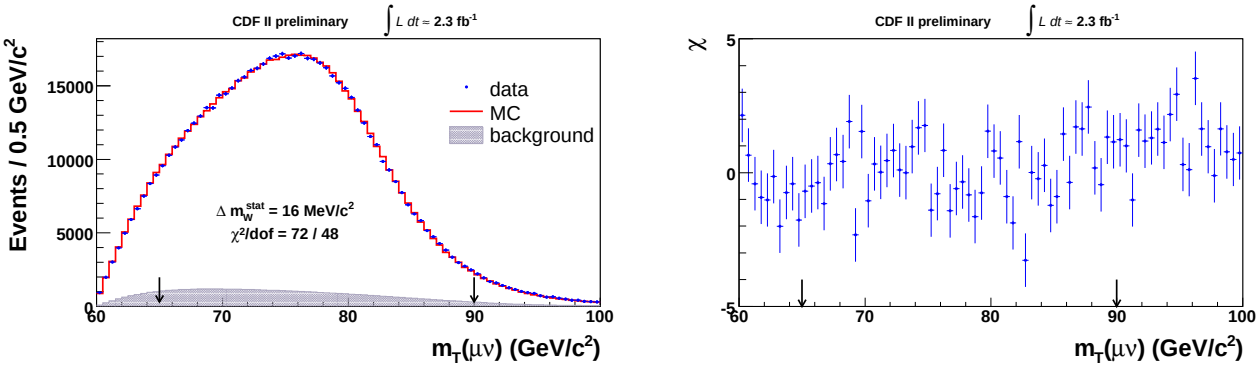

(a) (b)

Figure 7: (a) $W \to \mu\nu$ transverse mass fit, and (b) the difference between data and simulation (χ) in each bin, using `Simulation-I`. The fit range is $65 < m_T < 90\,\mathrm{GeV/c^2}$.

	χ^2	p.val.	$\Delta m_W^{\text{stat.}}(\text{MeV/c}^2)$
200 pb^{-1}	59/48	13 %	54
2300 pb^{-1}	72/48	1.4%	16

Table 10: $W \to \mu\nu$ transverse mass fit: the comparison of the fit quality and the statistical uncertainty on the fitted parameter (m_W) for the previous and current iteration.

7.2 $W \to e\nu$ m_T fit

The transverse mass m_T distribution is fitted to a sum of the estimated background contribution and a set of templates with different input m_W. The templates are generated at a fixed m_W, and then re-weighted according to the relativistic Breit-Wigner distribution (Eq. 8).

The fit result is obtained by maximizing the likelihood for the bins of the m_T distribution. The fitted value of m_W is blinded by the same unknown shift as in the case of the $W \to \mu\nu$ fits.

The background fractions and shapes are taken from Ref. [1].

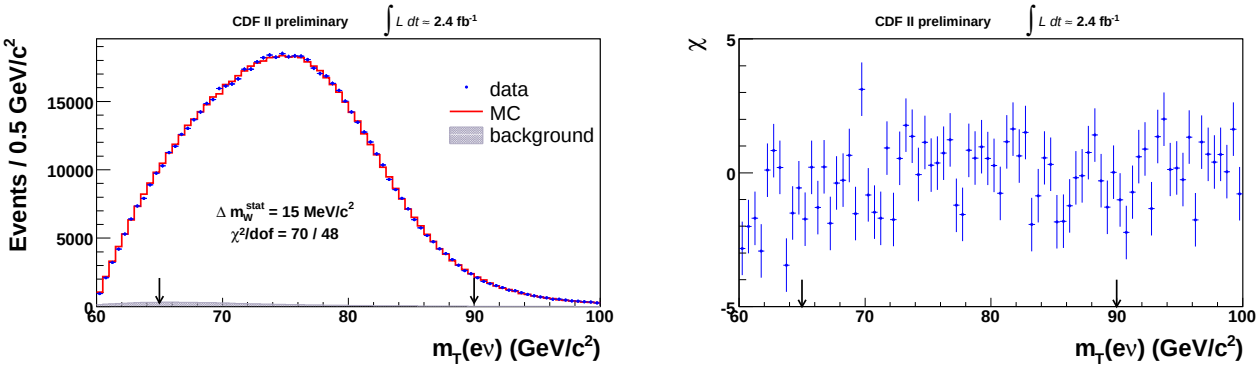

(a) (b)

Figure 8: (a) $W \to e\nu$ transverse mass fit, and (b) the difference between data and simulation (χ) in each bin, using `Simulation-I`. The fit range is $65 < m_T < 90\,\text{GeV/c}^2$.

	χ^2	p.val.	$\Delta m_W^{\text{stat.}}(\text{MeV/c}^2)$
200 pb^{-1}	86/48	0.1%	48
2400 pb^{-1}	75/48	0.8%	15

Table 11: $W \to e\nu$ transverse mass fit: the comparison of the fit quality and the statistical uncertainty on the fitted parameter (m_W) for the previous and current iteration.

7.3 $W \to e\nu$ E/pc fit

E/pc is the ratio between the energy of the electron, measured in the EM calorimeter, and its momentum, measured by fitting the track to the COT hits and the beam spot. It has a peak at 1 and a long tail at higher values, corresponding to the electrons that radiated photons before their momenta were measured, decreasing the measured momentum. The radiated photons often end up in the same calorimeter tower and are added back to the electron energy, hance causing the $E/pc > 1$ tail.

The E/pc distribution is sensitive both to the momentum and energy measurement parameters and is used to improve the energy scale determination by tuning the energy scale on the observed E/pc after the momentum scale has been applied.

The peak of the E/pc distribution is used to obtain the absolute energy scale, and the fits for the energy scale in bins of E_T are used to measure the non-linearity of the calorimeter response. The primary EM resolution parameter κ is also obtained from the χ^2 fit to the peak, while the material scale $S^{\rm mat}$ is tuned in the high E/pc tail on electrons that radiated when passing through detector material. It is therefore important to be able to accurately simulate E/pc shape.

We fit the E/pc distribution to a sum of templates with different absolute energy scales and the estimated background contribution. The statistical uncertainty in the fitted energy scale is propagated into an uncertainty of the m_W ($\Delta m_W^{\rm scale(stat.)} = 4{\rm MeV/c^2}$, see Fig. refFig-weveop).

For the fit presented in Fig. 9, we have retuned the material scale $S^{\rm mat}$ the contributions to the measured electron energy due to the underlying event, and have used the momentum scale from [1]. The calorimeter resolution parameters κ and κ_2 were also retuned (see Sec. 6.2).

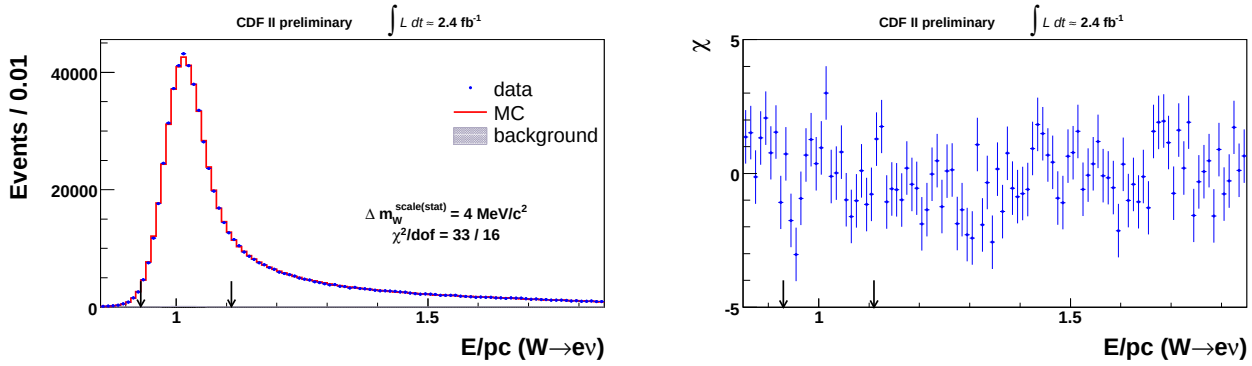

(a) (b)

Figure 9: (a) $W \to e\nu$ E/pc fit, and (b) the difference between data and simulation (χ) in each bin, using `Simulation-I`.

8 Conclusion

The fits to the kinematical distributions of the W, Z, J/ψ and $\Upsilon(1S)$ leptonic decays are presented using the fast simulations developed for the first CDF Run II W mass and width analyzes. After the first set of tunes and alignment corrections to the data they show a good description of distribution line shapes and the χ^2 values of the fits are already close to the ones obtained on 200 pb^{-1}(see Tables 7 to 6). The statistical uncertainties of the fitted parameters are scaling with statistics, showing that the degradation of the level of description due to the larger spread of instant luminosities and time-dependent effects has not significantly affected the sensitivity of the fits.

We propose to show the plots presented in the note, together with their χ^2 values and the statistical uncertainties of the fitted parameters, as an indicator of the status of the W mass analysis on 2.3 fb^{-1} of CDF Run II data.

References

[1] C. Hays, B. Jayatilaka, A. Kotwal, L. Nodulman, O. Stelzer-Chilton, W. Trischuk, I. Vollrath, CDF-NOTE-7104 (2006);
T. Aaltonen *et al.* [CDF Collaboration], *First Measurement of the W Boson Mass in Run II of the Tevatron*, Phys. Rev. Lett. **99**, 151801 (2007) [arXiv:0707.0085 [hep-ex]];
T. Aaltonen *et al.* [CDF Collaboration], *First Run II Measurement of the W Boson Mass*, arXiv:0708.3642 [hep-ex].

[2] V. Bartsch, D. Beecher, I. Bizjak, M. Lancaster, S. Malik, E. Nurse, T. Vine, D. Waters, CDF-NOTE-8668 (2006);
T. Aaltonen *et al.* [CDF Collaboration], *A direct Measurement of the W Boson Width in ppbar Collisions at sqrt(s) = 1.96 TeV*, Phys. Rev. Lett. **100**, 071801 (2008).

[3] C. Balazs and C.-P. Yuan, Phys. Rev. D **56** 5558 (1997).

[4] U. Baur, S. Keller, and D. Wackeroth, Phys. Rev. D **59** 013002 (1998).

[5] C.M. Carloni Calame, G. Montagna, O. Nicrosini and A. Vicini, *Precision electroweak calculation of the production of a high transverse-momentum lepton pair at hadron colliders*, JHEP 0710:109,2007 (arXiv:0710.1722 [hep-ph]),
C.M. Carloni Calame, G. Montagna, O. Nicrosini and A. Vicini, *Precision electroweak calculation of the charged current Drell-Yan process*, JHEP 0612 (2006) 016 (hep-ph/0609170).

[6] F. Landry, R. Brock, P. M. Nadolsky, and C. P. Yuan, Phys. Rev. D **67**, 073016 (2003).

[7] J. Pumplin, D. R. Stump, J. Huston, H. L. Lai, P. Nadolsky and W. K. Tung, JHEP **0207** (2002) 012.

[8] W. M. Yao *et al.* [Particle Data Group], J. Phys. G **33**, 1 (2006).

[9] T. Sjostrand, S. Mrenna and P. Skands, JHEP **0605**, 026 (2006) [arXiv:hep-ph/0603175].